Noname manuscript No.
(will be inserted by the editor)

Atlas-Based Fiber Reconstruction from Diffusion Tensor MRI Data

Sebastiano Barbieri · Jan Klein · Miriam H.A. Bauer · Christopher Nimsky · Horst K. Hahn

Received: date / Accepted: date

Abstract *Purpose:* Develop a neural fiber reconstruction method based on diffusion tensor imaging which is not as sensitive to user-defined regions of interest as streamline tractography.
Methods: A simulated annealing approach is employed to find a non-rigid transformation to map a fiber bundle from a fiber atlas to another fiber bundle which minimizes a specific energy functional. The energy functional describes how well the transformed fiber bundle fits the patient's diffusion tensor data.
Results: The feasibility of the method is demonstrated on a diffusion tensor software phantom. We analyze the behavior of the algorithm with respect to image noise and number of iterations. First results on the datasets of patients are presented.
Conclusions: The described method maps fiber bundles based on diffusion tensor data and shows high robustness to image noise. Future developments of the method should help simplify inter-subject comparisons of fiber bundles.

Keywords Diffusion Tensor Imaging · Fiber Tracking · Atlas · Registration

1 Introduction

Diffusion tensor imaging (see [6], [19]) is a magnetic resonance technique which measures the strength and direction of water molecule diffusion. Assuming that the main diffusion direction in an image voxel matches the average direction of the underlying fiber network, fiber tracking (FT) methods have been

S. Barbieri, J. Klein, H.K. Hahn
Fraunhofer MEVIS - Institute for Medical Image Computing
Universitätsallee 29, 28359 Bremen, Germany
E-mail: sebastiano.barbieri@mevis.fraunhofer.de

M.H.A. Bauer, Ch. Nimsky
Department of Neurosurgery, University of Marburg
Baldingerstrasse, 35033 Marburg, Germany

developed to reconstruct neural fiber bundles non-invasively and *in-vivo*. An overview of current tractography techniques can be found in [13]. Fiber tracking has increasingly gained acceptance as a pre- and intra-operative clinical tool used to determine, for example, positions of relevant neural tracts in relation to a tumor to be resected. In particular, streamline FT methods ([5], [17]), which start from a given region of interest (ROI) and propagate streamlines along the main diffusion directions of the diffusion tensors, enjoy widespread clinical use. This is possibly due to their quick computation times and the deterministic outputs they produce. A drawback of this type of algorithm is that the tracking result can be very sensitive with respect to the location and size of the starting ROIs chosen by the user [10]. Once the tracking has been performed, additional ROIs are often needed to exclude false positive streamlines, resulting in extensive post-processing operations.

In recent years, several atlas-based fiber reconstruction methods have been proposed. They are generally less dependent on user defined ROIs than streamline FT. These atlas-based methods start by computing a group averaged diffusion tensor image (DTI) which is then segmented to generate a parcellation map. The authors of [16] determine anatomical labels of cortex regions, manually at first and then in a refined manner via streamline tractography. Tract reconstruction is achieved by mapping the anatomical labels onto a patient's DTI and determining all streamlines with specific start and end regions. In [18], a white matter parcellation map (WMPM) is constructed by manually segmenting several tracts of interest based on the underlying color-coded orientation map. It is suggested that the WMPM can be registered to a patient's dataset to either automatically determine the location of specific tracts or as a reference for manual ROI-based segmentation. In [23, 24], streamline FT is employed on the averaged DTI, which is then registered onto the patient's DTI. For tract reconstruction, the registration transformation is applied to a binary mask derived from the tracked fibers.

In this work, we propose to start from a precomputed atlas of fiber bundles which are mapped onto the DTI data of the patient. In our opinion, focusing on mapping specific fiber bundles instead of a whole DTI should lead to computationally less expensive shape-consistent reconstructions. No post processing operations are needed once a fiber bundle has been "registered". Details about the suggested algorithm can be found in Section 2. Results of both synthetic and patient data are presented in Section 3. Current limitations and possible future improvements of the method are discussed in Section 4.

2 Methods

We now describe the proposed reconstruction approach. An overview of the algorithm and of how the individual steps are combined is presented in Algorithm 1.

2.1 Fiber Representation

In this article a "fiber bundle" F denotes a set of m fibers $\{f_j\}_{j=1,\ldots,m}$. We represent a fiber f_j as a tuple of n_j points:

$$f_j = (P_{1_j}, P_{2_j}, P_{3_j}, \ldots, P_{n_j}) \tag{1}$$

where P_{1_j} is the starting point of f_j and P_{n_j} its endpoint. Each fiber point is connected linearly to the next. Thus, we may associate a vector $\overrightarrow{v_{i_j}}$ to each fiber point P_{i_j} (but the endpoint), defined as

$$\mathbf{v_{i_j}} = P_{i+1_j} - P_{i_j} \text{ for } 1 \leq j \leq m, \text{ for } 1 \leq i < n_j\,. \tag{2}$$

Without loss of generality, we shall assume in the following that the distance between fiber points is constant. Whenever a transformation alters the distance between points, fibers are linearly resampled to maintain the assumption's validity.

2.2 Fiber Atlas

Our fiber atlas consists of various tracked fiber bundles. The tracking was performed based on the DTI data (resolution = $1.80 \times 1.80 \times 1.98$ mm^3, b value = 1000 s/mm^2, TR/TE = 12000/84 ms, two repetitions with one b=0 image and 30 gradient directions each) of a single healthy volunteer using the global approach by [15]. The tracked bundles include the arcuate fasciculus, the optic tracts, and fibers of the corticospinal tract originating from the hip, leg, hand, and face areas of the primary motor cortex (PMC).

2.3 Energy Functional

Consider a fiber bundle F from the fiber atlas and the diffusion tensor image $I : R^3 \to S^+(3,\mathbb{R})$, where $S^+(3,\mathbb{R})$ is the six-dimensional Riemannian manifold of 3×3 real symmetric positive-definite matrices. Our goal is to find a mapping Γ from a fiber bundle F to another fiber bundle $\Gamma(F)$ which minimizes a specific energy functional $E(\Gamma(F), I)$. In this work the mapping Γ preserves the number of tracked fibers but not necessarily their length (which, after resampling, corresponds to the number of points that define the individual fibers). The energy functional measures the match between the transformed fiber bundle and the main diffusion directions at the corresponding locations. It is defined as follows:

$$E(\Gamma(F), I) = \sum_{j=1}^{m} \frac{\sum_{i=1}^{n_j-1} \left(-\log\left(\mathbf{v_{i_j}}^T I(P_{i_j}) \mathbf{v_{i_j}}\right)\right)}{n_j - 1} \tag{3}$$

where ^{T} indicates the transpose operation, n_j indicates the number of points which define the j-th fiber and $I(P_i)$ is determined via nearest-neighbor interpolation. The energy functional is normalized with respect to the total number of fiber points.

In regions where two fiber bundles cross, diffusion tensors are generally disc-shaped. As no main diffusion direction is defined within this region, a minimization of the energy functional will not favor fibers running in a specific direction. The path of the mapped fiber bundle will instead be determined by the smoothness constraint imposed on the mapping Γ and by the main diffusion directions in regions adjacent to the fiber crossing. The same holds for a region infiltrated by a tumor and characterized by isotropic diffusion. However, the registration result is also influenced by the mean diffusivity in this region: if the mean diffusivity is high, a minimization of the energy functional will lead to fibers that go through the infiltrated region, if the mean diffusivity is low, fibers will bend around the tumor. Therefore, if the user is confident that fibers do not pass through a specific lesion (e.g. in the case of a metastasis), it may be useful to explicitly force fibers to bend around the lesion by weighting the corresponding diffusion tensors so that their mean diffusivity is decreased.

2.4 Simulated Annealing

To minimize the energy functional defined in Equation 3, we employ a strategy based on simulated annealing. Simulated annealing [14, 22] is a probabilistic metaheuristic: it iteratively adds a random perturbation to a given initial state. The decision to move to the new state depends on whether this state corresponds to a lower energy level or not and on the value of an artificial temperature variable $\mathcal{T}$ which decreases with each iteration. When the temperature is high, the decision to move to the new state is almost random; when the temperature decreases, "downhill" moves are increasingly favored. The main advantage of simulating annealing compared to "greedy" algorithms is that it is relatively robust with respect to solutions being trapped in local minima.

Depending on the fiber bundle to be reconstructed, we choose the corresponding tract from the fiber atlas and manually register it onto the patient's diffusion tensor image. During the manual registration process, we allow for the bundle to be translated, scaled, and rotated. The result is used as the initial state of the simulated annealing approach.

2.4.1 Candidate Generation

Next, we illustrate how the current state is perturbed during the simulated annealing process. Similarly to the initial manual registration step, we apply a combination of translation, scaling, and rotation to the current fiber bundle. However, within the suggested approach, these operations do not necessarily act globally on the whole fiber bundle, but may also have a "local" effect on

it, depending on a scale parameter σ_{scale}. The concatenation of "local" linear operations ultimately results in a non-rigid deformation of the original bundle from the fiber atlas. To apply one of the mentioned linear operations to the current fiber bundle, we start by randomly selecting (according to a uniform distribution) one fiber point, which we shall denote by P_{center_j} for a fixed j. This point corresponds to the location along the j-th fiber of the bundle, where the effect of the local transformation is the strongest. The transformation of the remaining points of the j-th fiber is computed depending on the points' distances to P_{center_j}. To compute a coherent transformation along the whole bundle, we determine the point which lies closest to P_{center_j} for each fiber. We thus obtain a center point for each fiber of the bundle and may assign a weight w_{i_j} to each fiber point. This weight determines the strength of the transformation at the point and is computed as follows:

$$w_{i_j} = \frac{\mathcal{G}(P_{i_j}, P_{\text{center}_j}, \sigma_{\text{scale}})}{\mathcal{G}(P_{\text{center}_j}, P_{\text{center}_j}, \sigma_{\text{scale}})} \text{ for } 1 \leq j \leq m, \text{ for } 1 \leq i \leq n_j \tag{4}$$

where $\mathcal{G}(\cdot, \mu, \sigma)$ denotes a Gaussian function with mean μ and standard deviation σ. The following sections detail how the single transformations are applied to the bundle.

Translation. The random translation magnitude $\mathbf{t}$ is sampled from the 3-D Gaussian distribution $\mathcal{N}(\cdot, \mathbf{0}, \sigma_{\text{translation}})$. The parameter $\sigma_{\text{translation}}$ reflects the expected magnitude. The translated points are determined according to

$$P'_{i_j} = P_{i_j} + w_{i_j} \cdot \mathbf{t} \tag{5}$$

Examples of global and local translations are displayed in Figs. 1(a) and 1(d).

Scaling. The random scaling magnitude $\mathbf{s}$ is sampled from the 3-D Gaussian distribution $\mathcal{N}(\cdot, \mathbf{1}, \sigma_{\text{scaling}})$. The parameter σ_{scaling} reflects the expected magnitude. The scaled points are determined in two steps. First, the scaling is applied to the vectors $\mathbf{v}_{i_j}$:

$$\mathbf{v}'_{i_j} = w_{i_j} \cdot \mathbf{s} * \mathbf{v}_{i_j} \tag{6}$$

where $*$ indicates the component-wise vector product. Next, the new position of the fiber points is determined via

$$P'_{i_j} = \begin{cases} P_{\text{center}_j} - \sum_{i'_j=i_j}^{\text{center}_j - 1} \mathbf{v}'_{i'_j} & \text{if } i_j \leq \text{center}_j \\ P_{\text{center}_j} + \sum_{i'_j=i_j}^{\text{center}_j} \mathbf{v}'_{i'_j} & \text{else} \end{cases} \tag{7}$$

Examples of global and local scalings are displayed in Figs. 1(b) and 1(e).

Rotation. The random rotation angle $\mathbf{r}$ is sampled from the 3-D Gaussian distribution $\mathcal{N}(\cdot, \mathbf{0}, \sigma_{\text{rotation}})$. The parameter σ_{rotation} reflects the expected magnitude of the rotation angles. The components of $\mathbf{r}$ represent the angles of rotation around the x-,y-, and z-axes, we weight them by w_{i_j} and determine

the corresponding rotation matrices R_x,R_y, and R_z at each fiber point. The rotated points are again determined in two steps. First, the rotation is applied to the vectors v_{i_j}:

$$\mathbf{v}'_{i_j} = R_x(w_{i_j} r_1)\, R_y(w_{i_j} r_2)\, R_z(w_{i_j} r_3)\, \mathbf{v}_{i_j} \tag{8}$$

Similar to the scaling transformation, the new positions of the fiber points are then determined according to Equation 7. Examples of global and local rotations are displayed in Figs. 1(c) and 1(f).

2.4.2 Cooling Schedule and Acceptance Probabilities

Denote the current iteration by *iter* and the maximum iteration number by $iter_{\max}$. The perturbed fiber bundle $\Gamma(F)$ corresponds to a new energy E_{new}. We keep track of the fiber bundle F_{best} corresponding to the overall lowest energy E_{best}. The current temperature $\mathcal{T}$ is computed as

$$\mathcal{T}(iter) = \exp\left(-10 \frac{iter}{iter_{\max}}\right). \tag{9}$$

The corresponding cooling schedule is illustrated in Fig. 2. The probability p of moving to the new state is computed as

$$p(\mathcal{T}) = \exp\left(\frac{E_{\text{old}} - E_{\text{new}}}{\mathcal{T}}\right). \tag{10}$$

If a random number r sampled from a uniform distribution over the interval $[0, 1]$ is smaller than p, the algorithm moves to the new state. Therefore, while the cooling process takes place, the likelihood of moving to a state which corresponds to a higher energy decreases. We always move to the new state if $E_{\text{new}} < E_{\text{old}}$. The simulated annealing process is repeated in a coarse-to-fine manner by using scale parameters of decreasing value $\sigma_{\text{scale big}}, \ldots, \sigma_{\text{scale small}}$.

2.5 Optional Transformation Restrictions

We mentioned that the initial state of the simulated annealing approach is given by a manual registration of the fiber bundle from the atlas onto the diffusion tensor image of the patient. Our confidence in the exactness of the manual registration result is likely to vary depending on the considered fiber tract and brain region. Where the manual registration result is believed to be correct, we may limit the effect of the transformation Γ on the current state F: the new state is given by F within user-defined ROIs, whereas we smoothly transition to $\Gamma(F)$ when moving away from these ROIs. For example, when reconstructing the corticospinal tract, we keep the manual registration result within the brainstem, or when reconstructing the optic tracts, we are generally able to locate the optic chiasm and therefore do not allow transformations in this region.

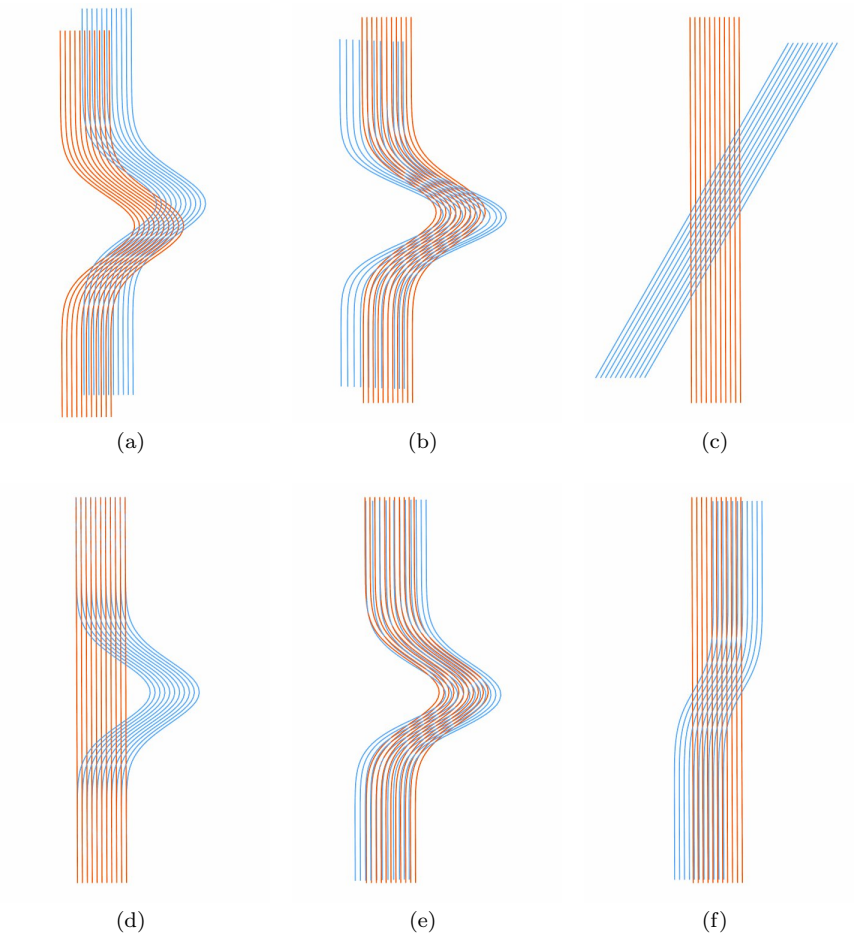

Fig. 1 Various transformations applied to an original fiber bundle displayed in orange. The result of the transformation is displayed in light blue. The length of the straight orange bundle in Fig. (d) is 80 mm, and the spacing between fibers is 1 mm. The top row shows global transformations, while the bottom row shows local transformations with $\sigma_{\text{scale}} = 40$ mm. In detail: (a) Global translation using $\mathbf{t} = (4.5, 4.5, 0)$ mm. (b) Global scaling using $\mathbf{s} = (1.4, 0.9, 0)$. (c) Global rotation using $\mathbf{r} = (0, 0, -30)°$. (d) Local translation using $\mathbf{t} = (15, 0, 0)$ mm. (e) Local scaling using $\mathbf{s} = (1.4, 0.9, 0)$. The transformation is centered where the fibers bend to the right. (f) Local rotation using $\mathbf{r} = (0, 0, -30)°$.

3 Results

We start by testing our algorithm on a DTI software phantom. The dataset is generated using control points and cubic spline interpolation as described in [3] and takes into account partial-volume artifacts between tensors. As suggested by [8], we simulate Rician distributed image noise by computing $|I_{\text{DW}} + \tilde{N}(0, \sigma_{\text{noise}})|$, where I_{DW} is the diffusion-weighted signal and $\tilde{N}(0, \sigma_{\text{noise}})$ is a Gaussian-distributed complex variable with mean 0 and standard devia-

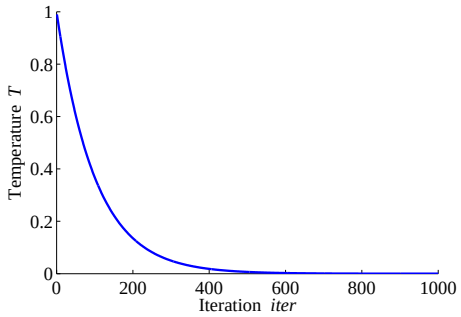

Fig. 2 The employed cooling schedule computed according to Equation 9. In this example, $iter_{\max} = 1000$.

tion σ_{noise}. Using standard fitting procedures, we compute the tensor-valued image based on the diffusion-weighted images. Table 1 reports the default parameters used to generate the DTI software phantom and to reconstruct the fiber bundle. Fig. 3 shows slices of the synthetic dataset in which the x-,y-, and z-components of the main diffusion direction have been mapped to red, green, and blue (RGB) color values, respectively. Figs. 3(a)-3(d) show various stages of the fiber reconstruction process. In Fig. 3(e), a second fiber bundle has been added to the synthetic dataset, resulting in a region of disc-shaped tensors where the fibers cross. Due to noise, the main diffusion direction in this region is basically random. The reconstruction result is very similar to the previous one-bundle example, indicating robustness of the algorithm with respect to fiber crossings. In Fig. 3(f), a tumor which is characterized by a low mean diffusivity and cuts into the synthetic fiber bundle has been simulated.

In Fig. 4(a), we report the lowest energy values E_{best} determined when reconstructing the fiber bundle with different levels of image noise. The standard deviation of the noise varies between 0 and 5.5 by increments of 0.5 (corresponding SNR between $+\infty$ and approximately 13), and for each standard deviation value, the reconstruction is repeated 10 times. The initial energy is approximately 0.3 for all experiments. In Fig. 4(b), we similarly vary the number of iterations used to reconstruct the fiber bundle. These range from 25 to 300 by increments of 25.

Next, we consider the diffusion tensor images of two patients. These datasets are publicly available from [11]. The parameters of the DTI acquisition sequence for the first patient are as follows: resolution $= 1.80 \times 1.80 \times 1.98$ mm^3, b value $= 1000$ s/mm^2, NEX $= 2$, TR/TE $= 10700/80$ ms, two repetitions with one b=0 image and 30 gradient directions each. The same parameters are used for the second patient but with TE=84 ms. The first patient is affected by intra-cerebral metastases. Reconstructions of part of the right corticospinal tract, of the optic tracts, and of the left arcuate fasciculus are presented in Fig. 5. Fig. 6 supports the claim that the transformed corticospinal tract better matches the underlying tensor data. The second patient is affected by a glioma. In Fig. 7, the part of the corticospinal tract originating from the hip

Algorithm 1 Algorithm for atlas- and DTI-based fiber reconstruction

Require: the relevant fiber bundle F from the fiber atlas
Require: maximum iteration number $iter_{\max}$
Require: scale parameters $[\sigma_{\text{scale big}}, \dots, \sigma_{\text{scale small}}]$
Require: transformation magnitude parameters $\sigma_{\text{translation}}$, σ_{scaling}, σ_{rotation}
{**Algorithm Start**}
{*Initialization*}
perform manual affine registration of F onto I
$F_{\text{best}} \leftarrow F$
$E_{\text{old}} \leftarrow E(F, I)$
$E_{\text{best}} \leftarrow E(F, I)$
{*Reconstruction Step*}
for $\sigma_{\text{scale}} \in [\sigma_{\text{scale big}}, \dots, \sigma_{\text{scale small}}]$ **do**
  for $iter = 1 \rightarrow iter_{\max}$ **do**
    select a transformation Γ between translation, scaling, and rotation
    compute $\Gamma(F)$ according to Section 2.4.1
    resample $\Gamma(F)$ with equidistant fiber points
    {*Compute corresponding energy*}
    $E_{\text{new}} \leftarrow E(\Gamma(F), I)$
    {*Decide whether to move to the new state*}
    select random r from uniform distribution over $[0, 1]$
    compute temperature $\mathcal{T}$ according to Eq. 9
    compute probability $p(\mathcal{T})$ according to Eq. 10
    if $r < p$ **then**
      $F \leftarrow \Gamma(F)$
      $E_{\text{old}} \leftarrow E_{\text{new}}$
      {*Check whether it is the best*}
      if $E_{\text{new}} < E_{\text{best}}$ **then**
        $F_{\text{best}} \leftarrow \Gamma(F)$
        $E_{\text{best}} \leftarrow E_{\text{new}}$
      end if
    end if
  end for
end for
return F_{best}
{**Algorithm End**}

and leg area of the PCM has been reconstructed and is compared to a streamline tractography result seeded within the internal capsule.

	Default value
noise standard deviation	2.5 (SNR=28)
radius of the bundle	13 mm
number of gradients	30
voxel size	$1 \times 1 \times 1$ mm^3
b value	1000 s/mm^2
noise-free $b = 0$ intensity	70
maximum iteration number	300
transformation scales	$[640, 320, 160, 80, 40]$ mm

Table 1 Default parameters used to generate the DTI software phantom and to reconstruct the fiber bundle.

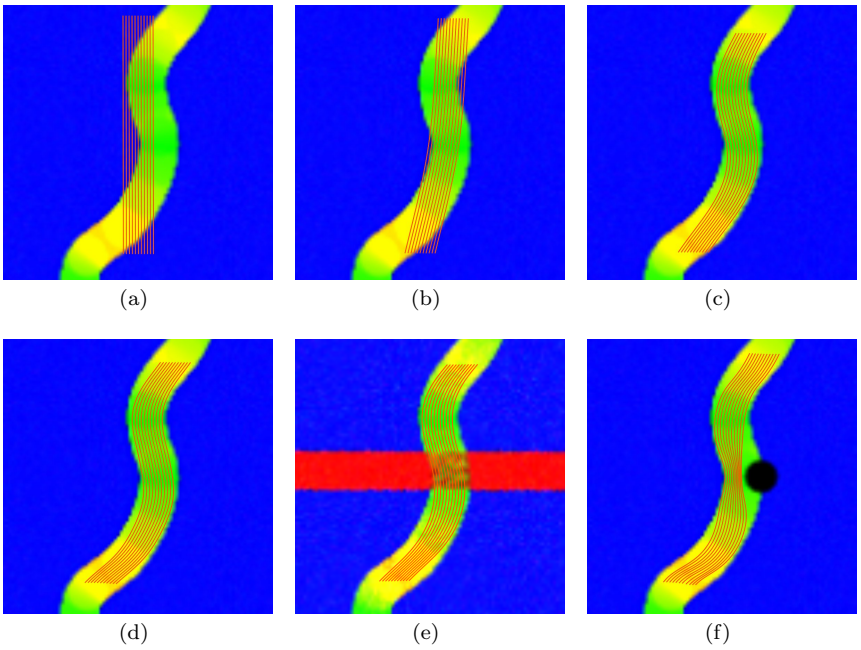

Fig. 3 Reconstruction of a synthetic fiber bundle. The size of the image is $100 \times 100 \times 40$ mm^3. (a) shows the fiber bundle initialization and a color-coding of the main diffusion directions of the tensor field. (b), (c) and (d) show subsequent reconstruction results after setting $\sigma_{\text{scale}} = 640$ mm, $\sigma_{\text{scale}} = 320$ mm, and $\sigma_{\text{scale}} = 40$ mm, respectively. (e) shows the reconstruction result after a crossing fiber bundle has been added to the synthetic dataset. In (f), a tumor which cuts into the synthetic fiber bundle has been simulated.

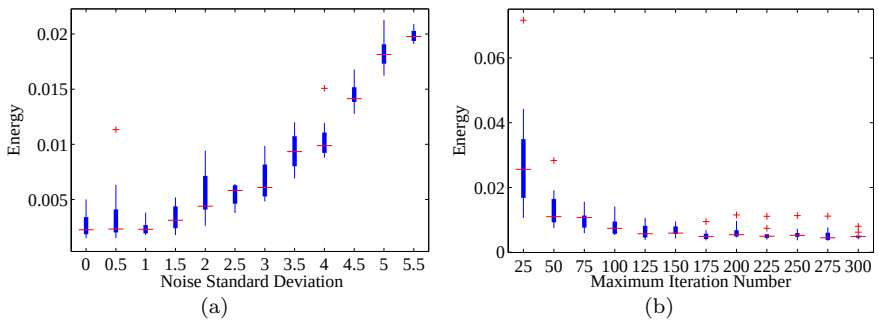

Fig. 4 Values of the lowest energy value E_{best} versus the standard deviation of the noise corrupting the DTI software phantom (a) and versus the maximum iteration number (b). The initial energy is approximately 0.3 for all experiments. The default parameters used to generate the phantom are reported in Table 1.

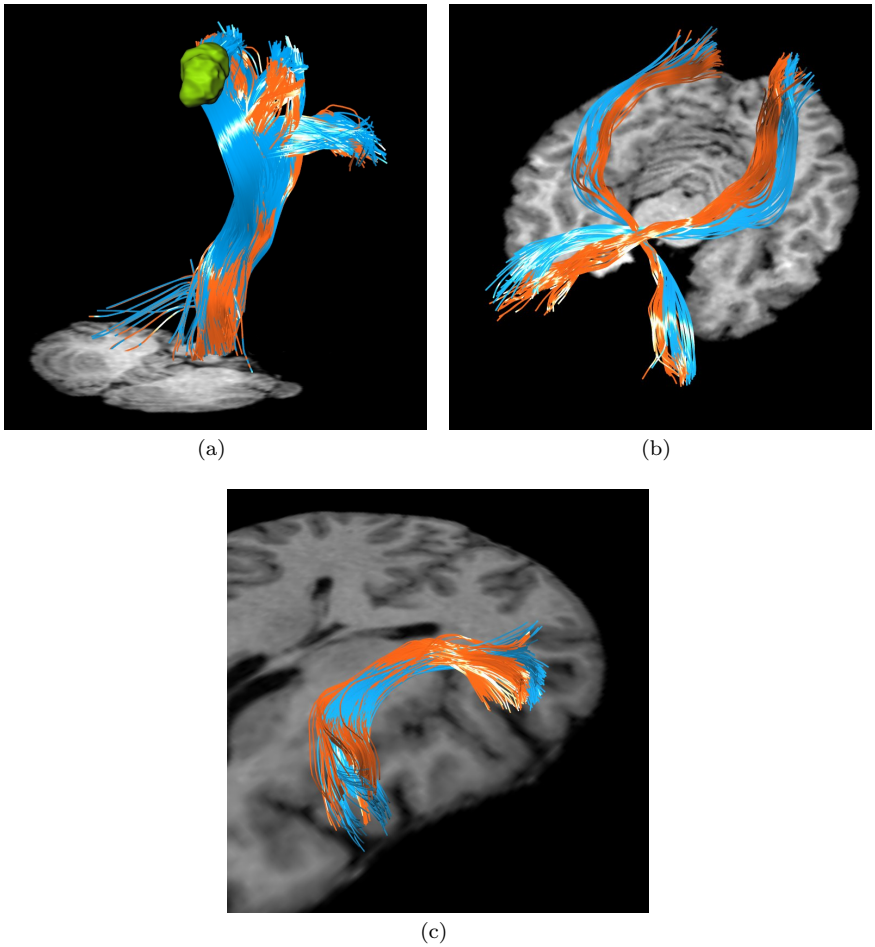

(a) (b)

(c)

Fig. 5 Reconstructions of the corticospinal tract (a) (hip and leg, hand, and face areas of the PMC), of the optic tracts (b), and of the arcuate fasciculus (c) of a patient with intra-cerebral metastases. The original fiber bundles from the fiber atlas are displayed in orange, while the transformed bundles are displayed in light blue. One of the metastases is shown in green.

4 Discussion

We have developed a method to map fiber bundles from a fiber atlas onto the DTI dataset of a patient. To the best of our knowledge, it is the first method to solve this specific problem. In the presented experiments, we start by performing a manual affine registration of the fiber bundles from the fiber atlas onto the DTI dataset of a patient. This step may be simplified in the future by employing automatic brain registration methods such as [9]. Next, in Equation 3, we formulate an energy functional to be minimized via a simulated annealing procedure. The energy value corresponds to how well the transformed fiber

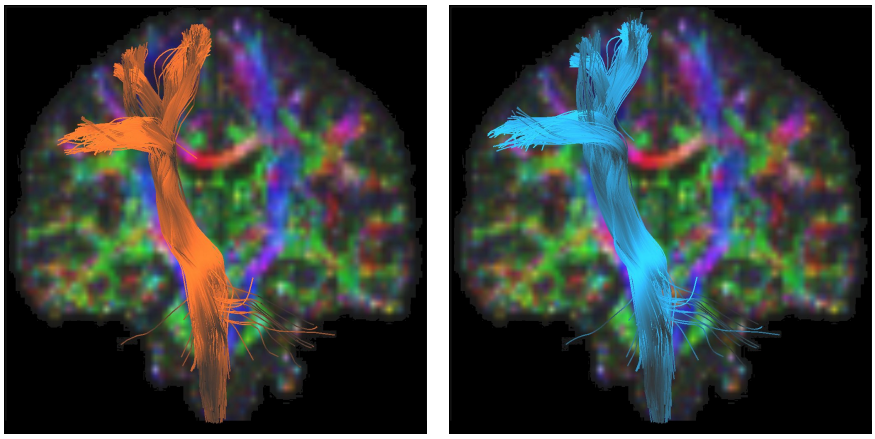

(a) (b)

Fig. 6 The corticospinal fibers presented in Fig. 5(a) are displayed on top of the color-coded diffusion tensor image before (a) and after (b) transformation.

bundle fits the underlying tensor data. Tensor values along the streamlines are so far determined by using nearest neighbor interpolation, although a future improvement could include linear or log-Euclidean [2] interpolation of the tensor data. Our approach operates in a multi-scale manner: it starts by applying global linear transformations to the fiber bundle, followed by more and more local transformations. The possibility of choosing the various transformation scales allows an elastic "registration" without running into over-fitting problems. Currently we perform a fixed number of iterations for each spatial scale. For future improvement, the computation time may be reduced by advancing to the next spatial scale when the energy decrease between successive iterations is smaller than a predefined threshold. Also, the possibility of simulating multiple cooldowns (instead of only one) at each spatial scale may be investigated. The final (backward) transformation of the fiber bundle from the atlas to the patient is given by a concatenation of linear operations applied to the fiber points and the line segments connecting them. Therefore, the inverse (forward) transformation from the patient to the atlas can be readily obtained if we track the center, scale, and type of applied transformations. Some inaccuracies in the forward transformation may arise due to the resampling, which keeps the distance between fiber points constant.

Fig. 3 illustrates the ability of the algorithm to deal with regions of low anisotropy (from either a fiber crossing or an infiltrating tumor) or with a tumor region where diffusion is low. When dealing with a non-infiltrating tumor (such as a metastasis), better results may be obtained by weighting the diffusion tensors by their fractional anisotropy so that regions of low anisotropy are severely penalized by the energy functional. In Fig. 4 we analyze the performance of the suggested approach on synthetic data when varying the level of image noise and the number of iterations. Because the energy functional

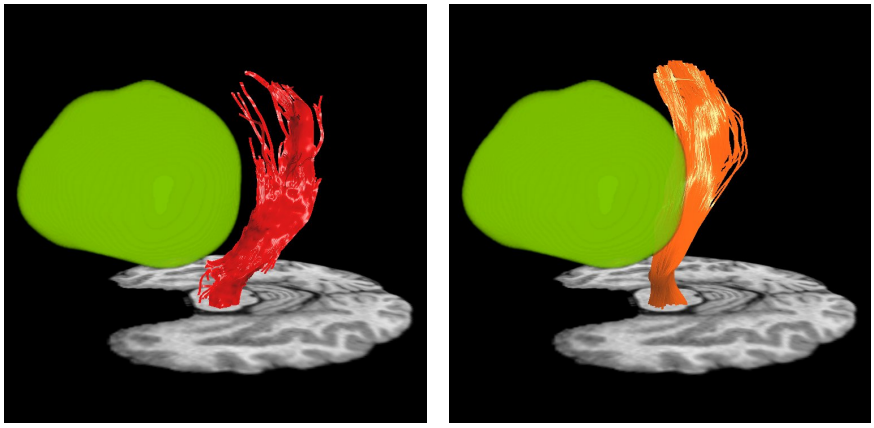

(a) (b)

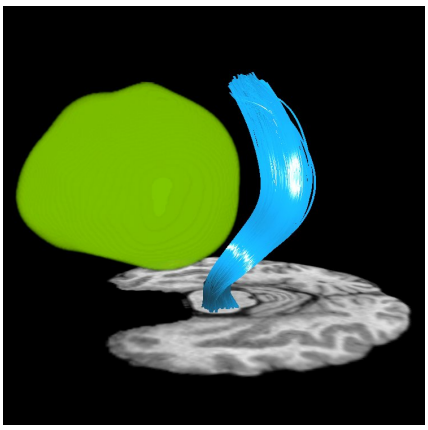

(c)

Fig. 7 (a) Reconstruction of the dominant part of the right corticospinal tract of a patient with glioma by means of streamline FT seeded within the internal capsule. The glioma is shown in green. Reconstruction via the proposed method is illustrated in (b) and (c). The original fiber bundles from the fiber atlas are displayed in orange, while the transformed bundles are displayed in light blue.

is computed globally on the whole fiber bundle, as expected the algorithm performs well also in the presence of considerable image noise. Approximately 150 iterations appear to be sufficient to reconstruct the fiber bundle on the given synthetic data. In Figs. 5 and 6, we present first reconstructions of the corticospinal tract, optic tracts, and arcuate fasciculus of a patient with intracerebral metastases. The optic tracts have been reconstructed simultaneously. If the user is interested in the simultaneous mapping of fiber bundles which vary considerably in size, it should be reasonable to weight the contributions to the energy functional according to the size of the bundles. Otherwise, large-scale transformations which provide a good fit for the larger bundles but not

for the smaller bundles could be accepted. Compared to streamline tractography approaches such as [5] and [17], the suggested approach does not require the user to define seed- or exclude-ROIs. However, we make use of ROIs to reduce the search space of possible transformations and reduce the risk of the simulated annealing approach terminating in a local minimum. Fig. 7 illustrates the reconstruction of a corticospinal tract considerably displaced by a glioma by means of our method. Visually the result is comparable to a reconstruction obtained by means of streamline FT seeded within the internal capsule.

The approach by the authors of [16] automatically determines the anatomical regions of the cortex to be used as start and end ROIs. This also leads their algorithm to be sensitive to inter-subject variability, because boundaries between regions may not necessarily be in the same position in different individuals. By relying on streamline FT, additional ROIs may still be needed to resolve crossing fibers or to eliminate fibers which continue into other pathways terminating into the same region. These operations are not needed with our algorithm. [18] presents a manually segmented white matter parcellation map which can be registered onto the DTI of a patient. Although very useful for anatomical orientation, the atlas can only provide a coarse fiber reconstruction, because often, only parts of fiber bundles could be delineated on the color-coded orientation map. In [23, 24], a DTI atlas is registered onto the DTI of a patient together with the binary mask derived from tracked streamlines. This appears to be a viable alternative for tract reconstruction without the need of user defined ROIs, however, it is restricted to non-branching sheet-like structures that can be effectively modeled by medial representations and may not be adequate to reconstruct fiber bundles which are considerably displaced due to lesions. Comparing the computational expense, we expect our algorithm to be faster: while the reconstructions presented in this paper took approximately 30 minutes to compute, the elastic registration of DTIs can be computationally quite expensive (compare [4]). Moreover, the effect of the transformation on the registered tensors poses a modeling challenge: while it is generally accepted that a rotation of the image leads to a rotation of the tensors (see [1]) it is not as clear what the effect of scaling or shearing the image should be. On the contrary, with our approach, we simply apply the transformation to the streamline defining points and interpolate them accordingly.

The employed fiber atlas is based on the data of a single subject. It would be interesting to create fiber atlases based on the tracked fiber bundles of multiple subjects, possibly grouped according to specific diseases. These atlases could consist either of averaged fiber bundles (the fiber bundle minimizing one of the distances between fiber bundles suggested by [12] could be determined) or of a map indicating the probability of a tract being in a specific location. With the latter option, a fiber tract could be reconstructed by considering its likelihood and the agreement of its trajectory with the diffusion data. The flexibility of the suggested approach could be increased by allowing the generation and the removal of streamlines. This would lead to a fiber tracking algorithm based

on global optimization, thus related to the work by [7] and [20] but without the need of generating fibers from a "soup of fragments", as prior knowledge about the expected shape of fibers can be incorporated. A preliminary step in this direction would probably consist in reformulating the problem in a continuous framework which starts from the definition of a streamline (a line whose tangent is always parallel to the vector field) and where the energy term considers both how well a streamline fits the underlying tensor data and how distant the streamline is from the atlas bundle. In the short term, if there is a considerable difference between the fiber bundles of the atlas and the patient, a landmark-based, thin-plate spline registration [21] could be used to initialize the simulated annealing process. Future work will also focus on applying the proposed method to High Angular Resolution Diffusion Imaging (HARDI, see [13, Chapter 4] for an overview), where in each voxel the probability that a diffusing water molecule moves in a particular direction is given by a probability density function sampled on the sphere. The energy functional will need to be modified to consider this probability (in the direction of the different vectors defining the streamlines) instead of the current vector norm defined by the diffusion tensor.

In conclusion, our hope is that this work may serve as a proof of concept for fiber reconstruction methods which map fiber bundles based on diffusion tensor data and which are not as sensitive to ROI placement as standard streamline tractography and will simplify inter-subject comparisons.

Acknowledgments

This project was funded in part by the German Research Society (DFG PE199/21-1 & DFG NI568/3-1). We would like to thank David Black for proof-reading this article.

References

1. Alexander, D., Pierpaoli, C., Basser, P., Gee, J.: Spatial transformations of diffusion tensor magnetic resonance images. IEEE Trans. Med. Imaging **20**(11), 1131–1139 (2001)
2. Arsigny, V., Fillard, P., Pennec, X., Ayache, N.: Log-euclidean metrics for fast and simple calculus on diffusion tensors. Magn. Reson. Med. **56**, 411–421 (2006)
3. Barbieri, S., Bauer, M., Klein, J., Nimsky, C., Hahn, H.: Segmentation of fiber tracts based on an accuracy analysis on diffusion tensor software phantoms. NeuroImage **55**(2), 532–544 (2011)
4. Barbieri, S., Welk, M., Weickert, J.: A variational approach to the registration of tensor-valued images. Springer, London, U.K. (2009)
5. Basser, P.: Fiber-tractography via diffusion tensor MRI (DT-MRI). In: Proc. Int. Soc. Magn. Reson. Med. (1998)
6. Basser, P., Mattiello, J., LeBihan, D.: MR diffusion tensor spectroscopy and imaging. Biophys. J. **66**(1), 259–267 (1994)
7. Fillard, P., Descoteaux, M., Goh, A., Gouttard, S., Jeurissen, B., Malcolm, J., Ramirez-Manzanares, A., Reisert, M., Sakaie, K., Tensaouti, F., Yo, T., Mangin, J.F., Poupon, C.: Quantitative evaluation of 10 tractography algorithms on a realistic diffusion MR phantom. Neuroimage **56**(1), 220–234 (2011)

8. Hahn, H., Klein, J., Nimsky, C., Rexilius, J., Peitgen, H.O.: Uncertainty in diffusion tensor based fibre tracking. Acta Neurochir. Suppl. **98**, 33–41 (2006)
9. Han, Y., Park, H.: Automatic registration of brain magnetic resonance images based on talairach reference system. Magn. Reson. Imaging **20**(4), 572–580 (2004)
10. Hattingen, E., Rathert, J., Jurcoane, A., Weidauer, S., Szelényi, A., Ogrezeanu, G., Seifert, V., Zanella, F., Gasser, T.: A standardised evaluation of pre-surgical imaging of the corticospinal tract: where to place the seed ROI? Neurosurg. Rev. **32**(4), 445–456 (2009)
11. Image Data, Case 1: http://viscontest.sdsc.edu/2010/ (2010)
12. Jiao, F., Phillips, J., Stinstra, J., Krüger, J., Varma, R., Hsu, E., Korenberg, J., Johnson, C.: Metrics for uncertainty analysis and visualization of diffusion tensor images. Lecture Notes in Computer Science **6326**, 179–190 (2010)
13. Johansen-Berg, H., Behrens, T.: Diffusion MRI. Academic Press, London, U.K. (2009)
14. Kirkpatrick, S., Gelatt, C.D., Vecchi, M.P.: Optimization by simulated annealing. Science **220**(4598), 671–680 (1983)
15. Klein, J., Köhler, B., Hahn, H.: Efficient global fiber tracking on multi-dimensional diffusion direction maps. In: Proc. SPIE Med. Imaging, vol. 8314, p. 83140M (2012)
16. Lawes, I., Barrick, T., Murugam, V., Spierings, N., Evans, D., Song, M., Clark, C.: Atlas-based segmentation of white matter tracts of the human brain using diffusion tensor tractography and comparison with classical dissection. Neuroimage **39**, 62–79 (2008)
17. Mori, S., Crain, B., Chacko, V., Van Zijl, P.: Three-dimensional tracking of axonal projections in the brain by magnetic resonance imaging. Ann. Neurol. **45**(2), 265–269 (1999)
18. Mori, S., Oishi, K., Jiang, H., Jiang, L., Li, X., Akhter, K., Hua, K., Faria, A., Mahmood, A., Woods, R., Toga, A., Pike, G., Neto, P., Evans, A., Zhang, J., Huang, H., Miller, M., van Zijl, P., Mazziotta, J.: Stereotaxic white matter atlas based on diffusion tensor imaging in an icbm template. Neuroimage **40**, 570–582 (2008)
19. Pierpaoli, C., Basser, P.: Toward a quantitative assessment of diffusion anisotropy. Magn. Reson. Med. **36**, 893–906 (1996)
20. Reisert, M., Mader, I., Anastasopoulos, C., Weigel, M., Schnell, S., Kiselev, V.: Global fiber reconstruction becomes practical. Neuroimage **54**(2), 955–962 (2010)
21. Rohr, K.: Landmark-Based Image Analysis. Kluwer Academic Press, Dordrecht, The Netherlands (2001)
22. Černý, V.: Thermodynamical approach to the traveling salesman problem: An efficient simulation algorithm. J. Optimization Theory and Appl. **45**, 41–51 (1985)
23. Yushkevich, P., Zhang, H., Simon, T., Gee, J.: Structure-specific statistical mapping of white matter tracts. Neuroimage **41**, 448–461 (2008)
24. Zhang, H., Awate, S., Das, S., Woo, J., Melhem, E., Gee, J., Yushkevich, P.: A tract-specific framework for white matter morphometry combining macroscopic and microscopic tract features. In: Proc. MICCAI, pp. 141–149 (2009)